https://doi.org/10.1038/s41567-019-0420-0

nature physics

Spin–phonon interactions in silicon carbide addressed by Gaussian acoustics

Samuel J. Whiteley[1,2,9], Gary Wolfowicz[1,3,9], Christopher P. Anderson[1,2], Alexandre Bourassa[1], He Ma[1,4], Meng Ye[1], Gerwin Koolstra[2,5], Kevin J. Satzinger[1,6], Martin V. Holt[7], F. Joseph Heremans[1,8], Andrew N. Cleland[1,8], David I. Schuster[2,5], Giulia Galli[1,4,8] and David D. Awschalom[1,8]*

Hybrid spin–mechanical systems provide a platform for integrating quantum registers and transducers. Efficient creation and control of such systems require a comprehensive understanding of the individual spin and mechanical components as well as their mutual interactions. Point defects in silicon carbide (SiC) offer long-lived, optically addressable spin registers in a wafer-scale material with low acoustic losses, making them natural candidates for integration with high-quality-factor mechanical resonators. Here, we show Gaussian focusing of a surface acoustic wave in SiC, characterized using a stroboscopic X-ray diffraction imaging technique, which delivers direct, strain amplitude information at nanoscale spatial resolution. Using ab initio calculations, we provide a more complete picture of spin–strain coupling for various defects in SiC with C_{3v} symmetry. This reveals the importance of shear strain for future device engineering and enhanced spin–mechanical coupling. We demonstrate all-optical detection of acoustic paramagnetic resonance without microwave magnetic fields, relevant for sensing applications. Finally, we show mechanically driven Autler–Townes splittings and magnetically forbidden Rabi oscillations. These results offer a basis for full strain control of three-level spin systems.

Hybrid quantum systems[1] can take advantage of the strengths of various modalities of representing quantum information, such as optical photons for sending quantum states across long distances, spins for information storage, and microwave superconducting circuits for computation, with the potential of using nanomechanics as an intermediary quantum bus. For instance, coherently exchanging quantum information between optically active defect spins and mechanical resonators[2] provides a route to couple optical photons to microwave frequency phonons in a hybrid quantum system. Optically active defect spins in SiC, such as the neutral divacancy[3], have recently been shown to support long-lived spin states[4–6], a variety of quantum controls[7], and spin–photon interfaces[8] compatible with quantum entanglement protocols. Importantly, SiC is a piezoelectric material and supports mature fabrication processes for production of high-quality microelectromechanical systems (MEMS). Although progress has been made coupling spins to mechanics in similar defect systems, including the nitrogen–vacancy centre in diamond with coherent sensing using single spins[9,10], strain tuning[11,12] and mechanical driving[13–16], defects in SiC are well positioned to solve the materials challenges of coherently manipulating spins with strain and strong coupling of spins with phonons.

While static strain will generate shifts in ground-state ($S=1$) energy sublevels, resonant a.c. strain can coherently drive electron spin transitions. Large in-plane dynamic strains can be generated by surface acoustic wave (SAW) devices, which are well developed for radiofrequency filters and offer simple engineering approaches for fabricating low-loss resonators. SAW devices have also been proposed as hybrid quantum transducers[17] and used to demonstrate coupling to superconducting qubits[18–20] along with optomechanical interactions involving defect excited states[21,22].

Here, we demonstrate acoustically driven $\Delta m_s=\pm1$ spin transitions, where $m_s=0,\pm1$ is the spin projection, on divacancy spin ensembles in 4H-SiC. We further demonstrate $\Delta m_s=\pm2$ spin transitions through the Autler–Townes effect, mechanical Rabi oscillations and comparing the relative coupling strengths of inequivalent divacancy defects. These results are well described by our theoretical model developed from a combination of direct experimental observations and density functional theory (DFT) calculations of anisotropic spin–strain coupling coefficients. We find that uniaxial and shear strains drive divacancy spins with coupling strengths of similar magnitude, but with generally different relative phase and selection rules. These experiments utilize a patterned Gaussian SAW phonon resonator that focuses strain and reduces resonator mode volumes in analogy to Gaussian optics. To image the mechanical modes of our Gaussian SAW devices, we use a unique nanoscale scanning X-ray diffraction technique that directly measures acoustic lattice perturbations. In addition, spatial responses of Autler–Townes splittings are well explained by ensemble-averaging shear and uniaxial strain from the SAW mode. Shear provides an important way of controlling three-level spins, called qutrits, with phonons and opens avenues for coupling spins with MEMS.

We first describe the device design and characterization with a nanoscale X-ray diffraction imaging method, followed by the spin manipulation. To amplify the piezoelectric response of the SiC substrate, we use a thin, sputtered aluminium nitride (AlN) layer on the SiC surface before fabricating a SAW resonator to create radiofrequency mechanical strain. Standard planar SAW resonator designs

[1]Institute for Molecular Engineering, University of Chicago, Chicago, IL, USA. [2]Department of Physics, University of Chicago, Chicago, IL, USA. [3]Advanced Institute for Materials Research, Tohoku University, Sendai, Japan. [4]Department of Chemistry, University of Chicago, Chicago, IL, USA. [5]The James Franck Institute, University of Chicago, Chicago, IL, USA. [6]Department of Physics, University of California, Santa Barbara, Santa Barbara, CA, USA. [7]Center for Nanoscale Materials, Argonne National Laboratory, Lemont, IL, USA. [8]Institute for Molecular Engineering and Materials Science Division, Argonne National Laboratory, Lemont, IL, USA. [9]These authors contributed equally: Samuel J. Whiteley, Gary Wolfowicz. *e-mail: awsch@uchicago.edu

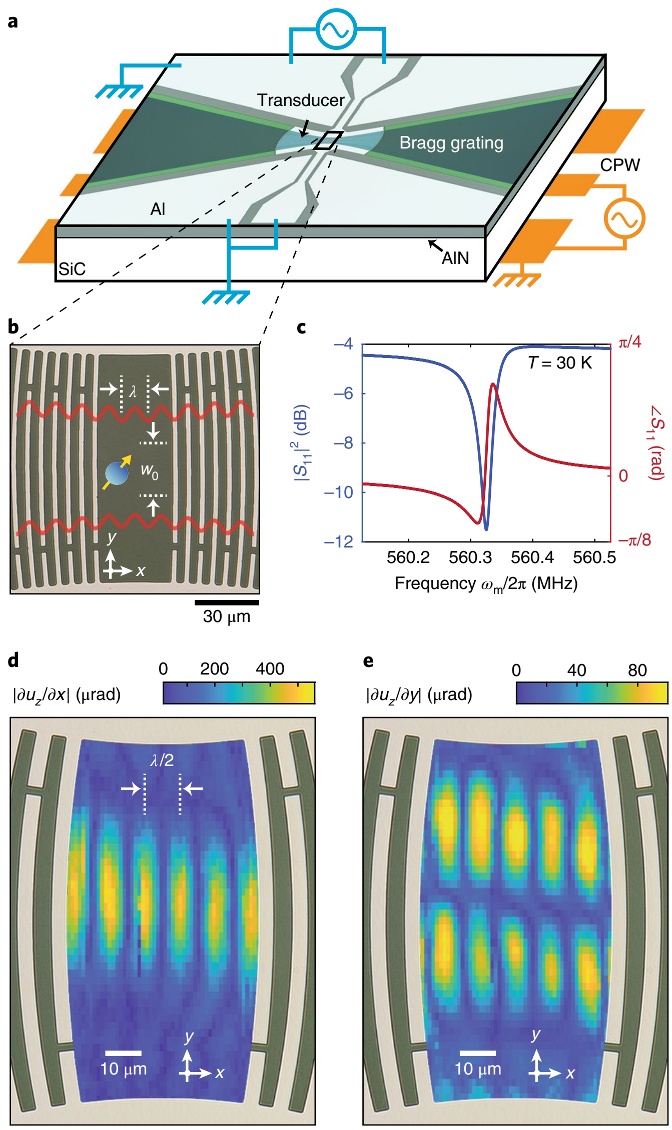

Fig. 1 | Strain focusing with a Gaussian SAW resonator. a, A schematic of the SAW device geometry fabricated on sputtered AlN on a 4H-SiC substrate. Microwaves drive spin transitions mechanically through the SAW resonator (cyan) and magnetically from the backside coplanar waveguide (orange). **b**, An optical micrograph of the Gaussian SAW resonator's acoustic focus ($\lambda = 12\,\mu$m, $w_0 = 2\lambda$) with red lines illustrating the wave's out-of-plane displacement (u_z). **c**, Magnitude (blue) and phase (red) measurements of the one-port reflection of the Gaussian SAW resonator used in spin experiments. **d**,**e**, The mechanical mode from a similar Gaussian SAW ($\lambda = 19\,\mu$m, $w_0 = 1.25\lambda$), directly measured with s-SXDM using the 4H-SiC [0004] Bragg peak. This quantifies the SAW peak-to-peak longitudinal (**d**) and transverse (**e**) lattice slopes at the acoustic beam waist. The image is skewed vertically due to sample drift during measurements.

span wide apertures, often greater than 100 acoustic wavelengths (λ), distributing the strain across large crystal areas. Since AlN and 4H-SiC have isotropic in-plane Rayleigh wave velocities[23] (5,790 and 6,830 m s^{-1}, respectively), we fabricate simple Gaussian geometries, inspired by Gaussian optics, to focus strain while also suppressing acoustic diffraction losses (Fig. 1a,b). A patterned aluminium interdigitated transducer transmits SAWs ($\lambda = 12\,\mu$m), while grooves in AlN form Bragg gratings that act as SAW cavity mirrors to support a resonator frequency $\omega_m/2\pi \approx 560$ MHz and loaded quality factor of ~16,000 (Fig. 1c) at 30 K. The Gaussian SAW resonator internal quality factor ($Q_i \approx 22{,}400$ at 30 K) is probably limited by the polycrystalline AlN layer at low temperatures (analysis shown in Supplementary Fig. 9). In our experiments, the Gaussian geometries for enhanced strain focusing and reduced resonator mode volumes facilitate larger strains for fast coherent manipulation of electron spin states.

To directly visualize the Gaussian mechanical mode, we use stroboscopic scanning X-ray diffraction microscopy[24] (s-SXDM) to image the phonons with nanoscale resolution. This technique utilizes coherent X-rays from a synchrotron radiation light source, generated at 8 keV and focused to a 25 nm spot size, and Bragg diffraction contrast to enable local measurements of lattice curvature and strain along a particular crystal orientation[25,26]. We match the radiofrequency excitation to a Gaussian interdigitated transducer with the timing structure of the synchrotron storage ring to measure the peak-to-peak amplitude of the acoustic standing wave. Due to the frequency-matching requirements for s-SXDM, we use a SAW transducer without a cavity (see Methods for device specifications), which is designed to produce a spatial strain mode similar to resonators used in spin experiments. Scanning the nano-focused X-ray beam in real space clearly shows that the SAW profile (Fig. 1d) is consistent with the fabricated geometry and approximately nanometre Rayleigh wave displacements. The dynamic transverse lattice slope (Fig. 1e), caused by a local lattice plane tilt towards the $\pm y$ direction, is expected from a Gaussian focus and SAW confinement. These X-ray measurements confirm that the SAW out-of-plane displacement (in phase with the in-plane uniaxial strain required for spin driving) is maximized at the resonator's precise centre and demonstrate the value of using X-ray diffraction microscopy for studying quantum devices[27] and materials.

Electron-spin ground-state sublevels of divacancy defects are typically measured using optically detected magnetic resonance (ODMR) with $\Delta m_s = \pm 1$ transitions magnetically driven by microwave fields. Due to the defect's intersystem crossing, ODMR probes the spin projections of $|\pm 1\rangle$ versus $|0\rangle$ through changes in photoluminescence. The ground-state spin Hamiltonian neglecting hyperfine interactions takes the form $H/h = \gamma \mathbf{B}\cdot\mathbf{S} + \mathbf{S}\cdot\mathbf{D}\cdot\mathbf{S}$, where h is the Planck constant, γ is the electron gyromagnetic ratio of approximately 2.8 MHz G^{-1}, $\mathbf{B}$ is the external magnetic field vector, $\mathbf{S}$ is the vector of Pauli spin-1 matrices and $\mathbf{D}$ is the zero-field splitting tensor. In the absence of lattice strain, the divacancy spin–spin interaction simplifies to $D_0 S_z^2$, where $D_0 \approx 1.336$ and 1.305 GHz, depicted in Fig. 2a, for c-axis-oriented defect configurations[28] hh and kk, respectively. The zero-field splitting is sensitive to local lattice perturbations[29] such as thermal disorder, an applied electric field or strain. When the lattice is perturbed by a small strain, characterized by a tensor ε_{kl}, the zero-field splitting tensor is generally modified by $\Delta D_{ij} = G_{ijkl}\varepsilon_{kl}$, where G_{ijkl} is the spin–strain coupling tensor. The symmetry of the spin–strain coupling tensor is determined by the local C_{3v} symmetry of the hh and kk configurations for divacancy (Supplementary Fig. 1) and also applies to the nitrogen–vacancy centre in diamond[30]. We utilize off-diagonal Hamiltonian elements containing ΔD_{ij} to drive resonant spin transitions with phonons, and consider both $\Delta m_s = \pm 1$ and ± 2 transitions for full ground-state $S = 1$ spin control.

We first demonstrate mechanical driving of $\Delta m_s = \pm 1$ spin transitions with the Gaussian SAW resonator. The point-group symmetries of the divacancy in SiC allow for non-zero spin–strain coupling coefficients for zero-field splitting terms that contain the anticommutators $\{S_x, S_z\}$ and $\{S_y, S_z\}$ (the derivation is in the Supplementary Information). To probe acoustic paramagnetic resonance, we tune the axial magnetic field (B_0) such that the spin $|0\rangle$ to $|-1\rangle$ transition frequency is matched with the SAW resonator (Fig. 2a). It is critical to design an experimental measurement sequence insensitive to stray magnetic fields from electrical currents in the interdigitated transducer. To disentangle these effects, we use an interlaced pump/laser probe sequence as well as lock-in amplification to measure the difference in luminescence when the spin resonance frequency is shifted away from the cavity resonance via modulation of B_0 with a small coil. Spin rotations are primarily driven and detected during the SAW cavity ring-down period without radiofrequency driving, although the spin ensemble will also encounter some residual magnetic resonance when the drive is turned back on due to lingering optical-spin polarization. We detect higher photoluminescence contrast when the radiofrequency drive is matched to our SAW cavity resonance (Fig. 2b), whereas smaller, residual contrast is detected when the drive is far off the SAW resonance. When the photoluminescence contrast is normalized by ODMR experiments from magnetic driving, the *kk/hh* mechanical drive rate ratio is 0.89 ± 0.10, which agrees with our theoretical model and DFT calculations (ratio ~1.0) where shear couples more strongly to $\Delta m_s = \pm 1$ transitions than does uniaxial strain (Supplementary Table 2). The transverse spatial dependence (Fig. 2c) confirms that the photoluminescence contrast we measure on resonance matches our Gaussian resonator's mechanical mode shape. Magnetic field driving from the transducer, on the other hand, results in a flat profile (two-dimensional spatial mapping is shown in Supplementary Fig. 3). The long cavity ring-up time prevents us from performing pulsed Rabi oscillations, although this could be solved using fast B_0 pulses to tune the spin resonance frequency. Our demonstration of $\Delta m_s = \pm 1$ transitions by phonons enables direct photoluminescence contrast (optical detection) of resonant spin–strain coupling for sensing applications without electromagnetic microwaves.

To complement $\Delta m_s = \pm 1$ spin driving, we further use the strain coupling terms $S_x^2 - S_y^2$ and $\{S_x, S_y\}$ in the zero-field splitting Hamiltonian to show $\Delta m_s = \pm 2$ spin transitions. For these transitions, photoluminescence contrast from ODMR cannot directly measure resonant strain without extra electromagnetically driven spin resonance because photoluminescence contrast is insensitive to differences between $|+1\rangle$ and $|-1\rangle$ states. The mechanical transition rate (Ω_m) is instead measured using Autler–Townes (a.c. stark) splittings, where in the dressed basis, the new eigenstates are split in energy by Ω_m. This splitting can be observed in the ODMR spectrum. We use a continuous magnetic microwave pump (Rabi frequency $\Omega_{B:\pm1} \approx$ MHz) for $|0\rangle$ to $|\pm1\rangle$ transitions while the SAW is driven at a constant frequency $\omega_m/2\pi$ (Fig. 3a). Dressed-state level anticrossings are most clearly seen when the $|\pm1\rangle$ spin sublevels are tuned to the SAW resonance frequency. The dressed spin eigenstate energies observed for a 400 mW drive power on the Gaussian SAW resonator closely match predictions[15] for $\Omega_m/2\pi \approx 4$ MHz (Fig. 3b). Moreover, the Autler–Townes splitting scales linearly with the square root of the radiofrequency drive power delivered to the SAW, which is expected as Ω_m is linearly proportional to strain (Fig. 3c). The resolved Autler–Townes splitting shows that the mechanical drive rate is faster than the ensemble spin inhomogeneous linewidth (decoherence rate), allowing for measurement of coherent Rabi oscillations.

We mechanically drive coherent Rabi oscillations of *kk* electron spins using the pulse sequence in Fig. 3d to differentiate between populations transferred to $|+1\rangle$ versus $|-1\rangle$ spin states. The spin ensemble inhomogeneous linewidth (~1 MHz) and relatively long cavity ring-up time ($2Q/\omega_m \approx 16$ µs) prevent fast mechanical pulsing, so we keep the mechanical drive on continuously. A pair of magnetic microwave π pulses defines the effective mechanical pulse time τ seen by the spin ensemble (Fig. 3d). Using this pulse sequence and positive ODMR contrast of *kk* defects, normalized photoluminescence values of ±1 can be interpreted as $|\mp1\rangle$ spin populations, respectively, before the second magnetic π pulse. We find that three-level system dynamics are necessary to explain the observed mechanical Rabi oscillations shown in Fig. 3e, in particular the

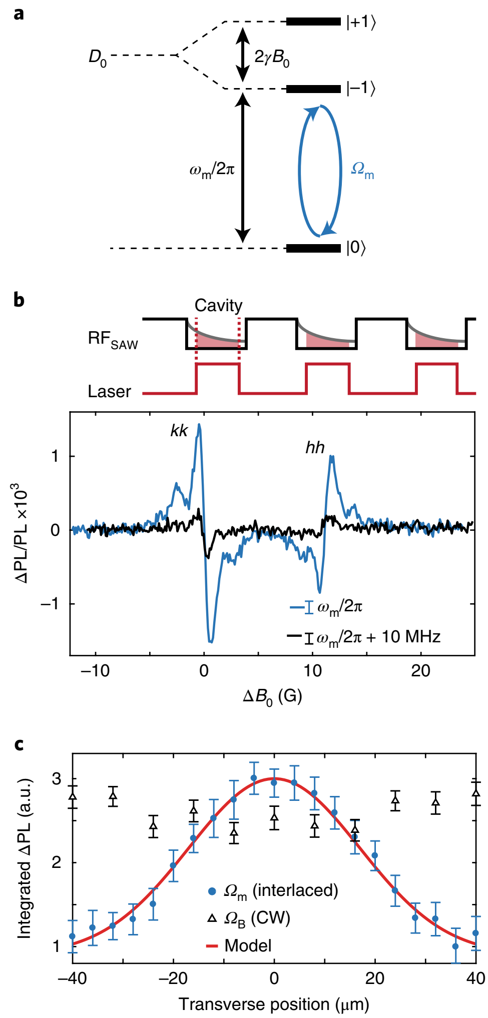

Fig. 2 | Optically detected acoustic paramagnetic resonance in silicon carbide. a, An energy-level diagram showing the SAW frequency on resonance with the spin transition between the $|0\rangle$ and $|-1\rangle$ states. **b**, Top: interlaced pump–probe sequence during magnetic field modulation. Bottom: photoluminescence (PL) contrast at 30 K when electrical excitation is on and off cavity resonance ($\omega_m/2\pi = 559.6$ MHz). The radiofrequency power is 32 mW at the sample, and ΔB_0 is in reference to the drive frequency. **c**, Integrated photoluminescence contrast from *kk* resonance (evaluated at $\Delta B_0 = 0$) as a function of the SAW resonator transverse position. Driving on resonance (Ω_m) uses the interlaced sequence from **b**, whereas off-resonance data (Ω_B) use a continuous, non-interlaced sequence. The radiofrequency power is 200 mW at the sample, and the beam waist model is $\exp\left(\frac{-y^2}{w_0^2}\right)$, using fabrication parameters and a scaled amplitude. All error bars are 95% confidence intervals.

ensemble population at $\tau = 0$. Specifically, during each magnetic π pulse, the simultaneous mechanics Ω_m drives some unintended population transfer between the $|+1\rangle$ and $|-1\rangle$ spin states, which leads to a modified initial projection of the population at $\tau = 0$.

The observed Rabi oscillations qualitatively agree with spin simulations predicted using a physical model consisting of spin–strain coupling parameters from DFT calculations and experimental knowledge, including: the ensemble spin resonance spectrum from ODMR; spin–mechanical drive amplitudes from fitted Autler–Townes splittings; spatial distribution of spins in the SiC bulk and implanted layer; finite-element analysis of strain and shear distributions from Rayleigh waves; and optical point-spread

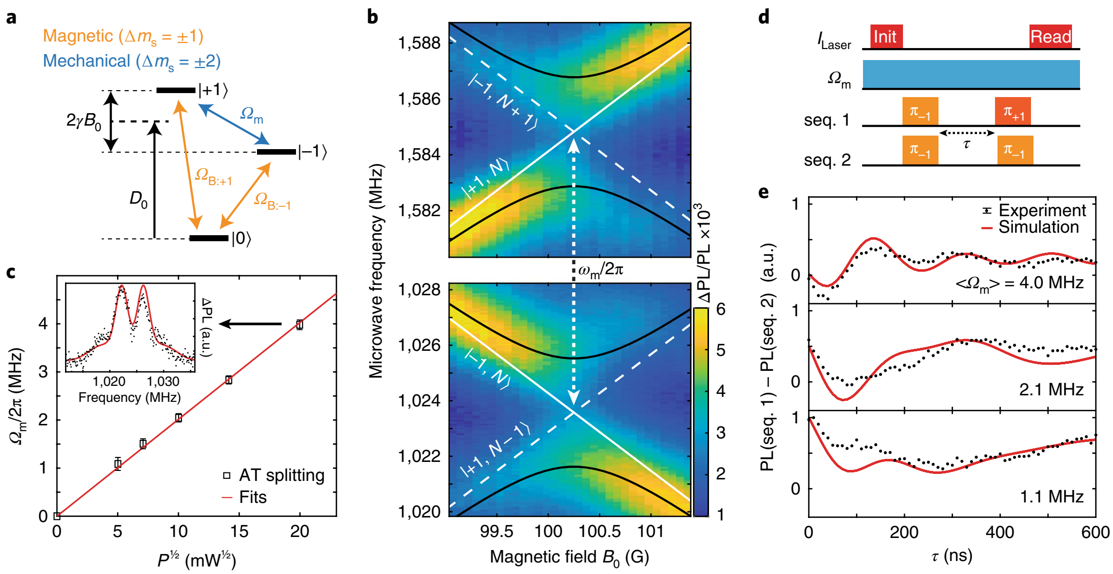

Fig. 3 | Coherent mechanical driving of *kk* spin ensembles. a, A divacancy ground-state illustration with magnetic ($\Omega_{B:\pm1}$) and electromechanical (Ω_m) drives shown. **b**, Autler–Townes measurement on a *kk* ensemble at 30 K; dressed for *N* phonons (black) and undressed (white) spin transitions. The mechanically dressed eigenstates and corresponding transitions are split by Ω_m. **c**, Mechanical transition rates obtained from Autler–Townes (AT) splittings agree with a linear fit to the square root of the drive power. The error bars are 95% confidence intervals from fits. The inset shows an Autler–Townes splitting measurement (black) at $B_0\approx100$ G, with Gaussian fits (red) to the divacancy electron spin and weakly coupled nearby nuclear spins. **d**, Pulse sequence for mechanically driven Rabi oscillations. **e**, Mechanically driven Rabi oscillations at ~400, 100 and 25 mW, respectively, and the error bar in the legend is the average 95% confidence interval of each experimental data point. The photoluminescence signal for each Rabi oscillation is normalized by a global factor, and simulations are ensemble-average predictions with inhomogeneous strain distributions from finite-element modelling.

function (Supplementary Fig. 5). Our physical model reproduces the mechanically driven Rabi oscillation rates, asymmetric decay shape, higher-frequency features from hyperfine detuned spins and initial spin population at $\tau=0$. This demonstrates that we can mechanically drive $\Delta m_s=\pm2$ transitions with a Rabi frequency about 4 times greater than the ensemble ODMR linewidth. During Rabi oscillations with 400 mW radiofrequency power, we estimate from input–output theory applied on a SAW model (the derivation is shown in the Supplementary Information) that the mechanical field strength is approximately 10^{-3} strain order of magnitude, in agreement with DFT simulation results. Short Rabi decay times are primarily explained by SAW strain inhomogeneity across the ensemble, although another source of damping may be present in the experiments. Manipulation of single divacancies[4,8] will offer the opportunity to extend coherent Rabi oscillations up to or beyond the spin T_2^*. Coherent Rabi oscillations in ensembles for quantum phononics applications could be improved by using higher-quality material and controlled aperture implantations[31] for more homogeneous strain distributions.

We spatially map the Gaussian SAW mode to show that $\Delta m_s=\pm2$ transitions occur due to the mechanical driving and not due to any stray electromagnetic fields[32]. We map changes in the Autler–Townes splitting, shown in Fig. 4a, at a constant magnetic field while sweeping the laser position across the SAW beam waist. In the resonator's transverse direction, a clear Autler–Townes splitting maximum, and therefore resonant strain amplitude, is observed at the Gaussian acoustic focus. Ω_m as a function of transverse position is well described by a model Gaussian beam waist of the fundamental mode in the device geometry (full-width at half-maxium $=3.3\lambda$) and not due to predicted stray electric fields (Supplementary Fig. 4). Scanning the laser spot longitudinally (Fig. 4b), along the SAW propagation, reveals oscillations in the Autler–Townes splitting at the resonator's acoustic half-wavelength. Surprisingly, in conflict with assumptions of a simple sinusoidal standing wave containing uniaxial strain nodes (Fig. 1d,e), we observe that the mechanical drive rate oscillations are less than 5% peak-to-peak. This is in contrast to expectations from previous theoretical work[33] neglecting the full strain tensor, so we interpret our experimental results using a spin Hamiltonian under anisotropic strains also including shear.

The spatial mapping results can be understood by employing a combination of finite-element simulations in conjunction with DFT calculations of spin–strain interactions (see Supplementary Information). The $\{11\bar{2}0\}$ mirror-plane symmetry in 4H-SiC is broken by shears ε_{xz} and ε_{xy}, which drive the spin out-of-phase with $\varepsilon_{xx}-\varepsilon_{yy},\varepsilon_{yz}$ (mirror-symmetry-preserving). In our experiments, the Gaussian SAW beam waist is oriented to propagate in the $\{1\bar{1}00\}$ plane (defined as the *xz* plane). The mechanical transition rate is $\Omega_m=\frac{1}{2}(G_{11}-G_{12})\varepsilon_{xx}-2iG_{14}\varepsilon_{xz}$ corresponding to $\Delta m_s=\pm2$ transitions, where the spin–strain coupling tensor *G* is written in Voigt notation. In Fig. 4c, we show finite-element simulation results for uniaxial strain ε_{xx} and shear ε_{xz} for a Rayleigh wave propagating along the *x* direction. We model the experimental results by converting the strain maps to Ω_m using *G* calculated from DFT, which is then convolved with both an optical point-spread function and estimated spatial distribution of the spins (Supplementary Fig. 5). In our model, spatial averaging causes the spin ensemble to experience similar transition rate Ω_m magnitudes from $(G_{11}-G_{12})\varepsilon_{xx}$ and $G_{14}\varepsilon_{xz}$ contributions at their respective spatial maxima. These uniaxial strain and shear components, which are spatially offset, do not interfere destructively since Ω_m is proportional to a linear combination of $\varepsilon_{xx}(S_x^2-S_y^2)$ and $\varepsilon_{xz}(S_xS_y+S_yS_x)$. Consequently, in qualitative agreement with our calculations (Supplementary Fig. 6), we always experimentally measure a non-zero Autler–Townes splitting in Fig. 4b. Furthermore, our model explains the relative Ω_m amplitudes between *kk* and *hh* (4.0:1.1) observed in Fig. 4d, and the results for $\Delta m_s=\pm2$ transitions are well described by the zero-field splitting tensor when the full strain tensor is taken into account. Lastly, we measure mechanical spin driving on the PL6 defect species in SiC, previously used to demonstrate electron–nuclear spin entanglement

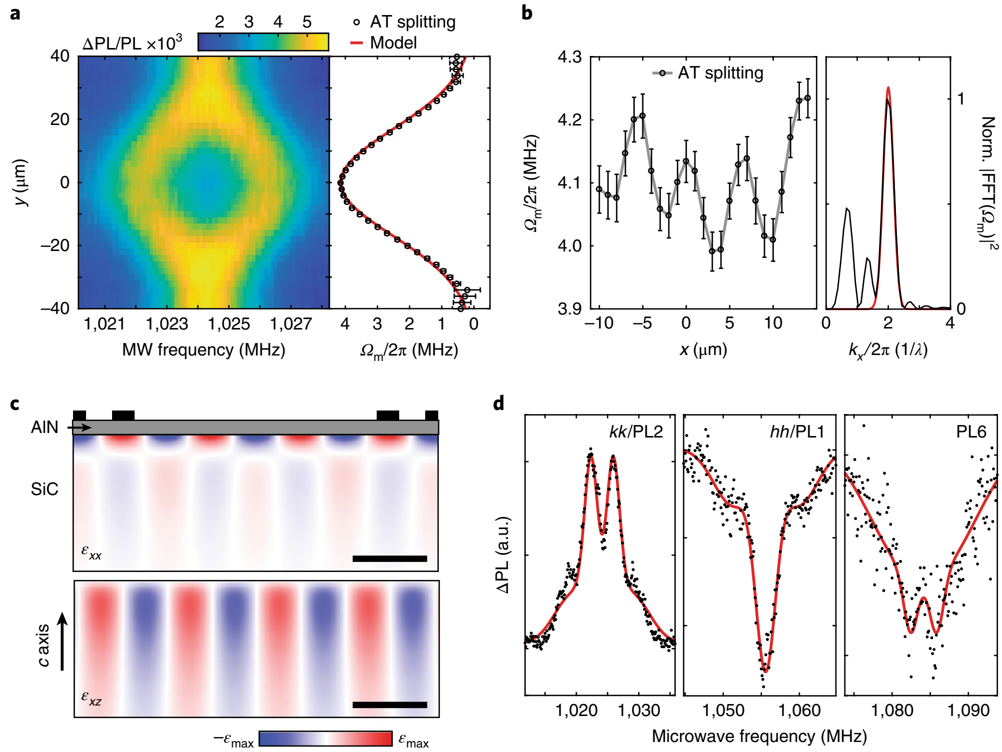

Fig. 4 | Spatially mapping mechanical spin drive rates and defect comparisons. a, Autler–Townes splitting (left) of the *kk* $|-1\rangle$ sublevel as a function of transverse position at $x=0$ and mechanical transition rate (right) analysed from Autler–Townes splittings. The beam waist model uses only fabrication parameters with a scaled amplitude. **b**, Mechanical transition rate (left) as a function of longitudinal position at $y=0$, plotted with a line through the experimental data. The fast Fourier transform (FFT; right) shows a peak and Gaussian fit in red at the expected acoustic periodicity $\lambda/2$ (6 μm). **c**, Strain ε_{xx} and ε_{xz} of the SAW modelled with COMSOL Multiphysics. **d**, Autler–Townes splitting measurements (black points) for *kk*, *hh* and PL6 with $\Omega_m \sim 4.0$, 1.1 and 3.4 MHz, respectively, under the same conditions. The fits (red lines) are from simultaneously fitting the data with ODMR spectra to common Gaussian distributions (Supplementary Fig. 8). All error bars are 95% confidence intervals from fitting and measurements are performed at 30 K.

in ambient conditions[34]. We find that PL6 experiences similar mechanical transition rates compared to *hh* and *kk* (Fig. 4d); therefore, mechanical control of SiC spin ensembles should be possible at room temperature.

Since a complete model of spin–strain coupling with C_{3v} symmetry requires six independent coupling parameters, strain cannot necessarily be treated as an equivalent electric field vector. Even so, the zero-field splitting tensor is also affected by electric fields with three independent coupling parameters and can be used for both $\Delta m_s = \pm1$ and $\Delta m_s = \pm2$ spin transitions. To further enhance defect–phonon interaction strengths for hybrid quantum systems, defect excited-state electronic orbitals[35,36] and spins[37] could be utilized as opposed to ground-state spins[38], and strain effects on defect hyperfine couplings have not been well explored. In addition, new defects[39] with greater spin–spin or spin–orbit coupling, with minimal cost to their spin coherence, may greatly improve spin–phonon coupling strengths and be advantageous for quantum control of phonons with optically addressable spins. Our combined theoretical understanding and demonstrations of spin–strain coupling with SiC divacancies provides a basis for quantum sensing with MEMS[40] as well as engineering strong interactions with single phonons for quantum transduction[1], spin squeezing[41] and phonon cooling[42] applications.

Online content

Any methods, additional references, Nature Research reporting summaries, source data, statements of data availability and associated accession codes are available at https://doi.org/10.1038/s41567-019-0420-0.

Received: 27 July 2018; Accepted: 7 January 2019;
Published online: 11 February 2019

References

1. Kurizki, G. et al. Quantum technologies with hybrid systems. *Proc. Natl Acad. Sci. USA* **112**, 3866–3873 (2015).
2. Lee, D., Lee, K. W., Cady, J. V., Ovartchaiyapong, P. & Bleszynski Jayich, A. C. Topical review: spins and mechanics in diamond. *J. Opt.* **19**, 033001 (2017).
3. Koehl, W. F. et al. Room temperature coherent control of defect spin qubits in silicon carbide. *Nature* **479**, 84–87 (2011).
4. Christle, D. J. et al. Isolated electron spins in silicon carbide with millisecond coherence times. *Nat. Mater.* **14**, 160–163 (2015).
5. Widmann, M. et al. Coherent control of single spins in silicon carbide at room temperature. *Nat. Mater.* **14**, 164–168 (2015).
6. Seo, H. et al. Quantum decoherence dynamics of divacancy spins in silicon carbide. *Nat. Commun.* **7**, 12935 (2016).
7. Heremans, F. J., Yale, C. G. & Awschalom, D. D. Control of spin defects in wide-bandgap semiconductors for quantum technologies. *Proc. IEEE* **104**, 2009–2023 (2016).
8. Christle, D. J. et al. Isolated spin qubits in SiC with a high-fidelity infrared spin-to-photon interface. *Phys. Rev. X* **7**, 021046 (2017).
9. Kolkowitz, S. et al. Coherent sensing of a mechanical resonator with a single-spin qubit. *Science* **335**, 1603–1606 (2012).
10. Hong, S. et al. Coherent, mechanical control of a single electronic spin. *Nano. Lett.* **12**, 3920–3924 (2012).
11. Teissier, J., Barfuss, A., Appel, P., Neu, E. & Maletinsky, P. Strain coupling of a nitrogen-vacancy center spin to a diamond mechanical oscillator. *Phys. Rev. Lett.* **113**, 020503 (2014).
12. Ovartchaiyapong, P., Lee, K. W., Myers, B. A. & Bleszynski Jayich, A. C. Dynamic strain-mediated coupling of a single diamond spin to a mechanical resonator. *Nat. Commun.* **5**, 4429 (2014).
13. MacQuarrie, E. R. et al. Coherent control of a nitrogen-vacancy center spin ensemble with a diamond mechanical resonator. *Optica* **2**, 233–238 (2015).

14. Barfuss, A., Teissier, J., Neu, E., Nunnenkamp, A. & Maletinsky, P. Strong mechanical driving of a single electron spin. *Nat. Phys.* **11**, 820–824 (2015).
15. MacQuarrie, E. R., Gosavi, T. A., Bhave, S. A. & Fuchs, G. D. Continuous dynamical decoupling of a single diamond nitrogen-vacancy center spin with a mechanical resonator. *Phys. Rev. B* **92**, 224419 (2015).
16. Barfuss, A. et al. Phase-controlled coherent dynamics of a single-spin under closed-contour interactions. *Nat. Phys.* **14**, 1087–1091 (2018).
17. Schuetz, M. J. A. et al. Universal quantum transducers based on surface acoustic waves. *Phys. Rev. X* **5**, 031031 (2015).
18. Manenti, R. et al. Circuit quantum acoustodynamics with surface acoustic waves. *Nat. Commun.* **8**, 975 (2017).
19. Moores, B. A., Sletten, L. R., Viennot, J. J. & Lehnert, K. W. Cavity quantum acoustic device in the multimode strong coupling regime. *Phys. Rev. Lett.* **120**, 227701 (2018).
20. Satzinger, K. J. et al. Quantum control of surface acoustic-wave phonons. *Nature* **563**, 661–665 (2018).
21. Golter, D. A., Oo, T., Amezcua, M., Stewart, K. A. & Wang, H. Optomechanical quantum control of a nitrogen-vacancy center in diamond. *Phys. Rev. Lett.* **116**, 143602 (2016).
22. Golter, D. A. et al. Coupling a surface acoustic wave to an electron spin in diamond via a dark state. *Phys. Rev. X* **6**, 041060 (2016).
23. Takagaki, Y. et al. Guided propagation of surface acoustic waves in AlN and GaN films grown on 4H-SiC (0001) substrates. *Phys. Rev. B* **66**, 155439 (2002).
24. Whiteley, S. J., Heremans, F. J., Wolfowicz, G., Awschalom, D. D. & Holt, M. V. Imaging dynamically-driven strain at the nanometer-scale using stroboscopic scanning X-ray diffraction microscopy. Preprint at https://arxiv.org/abs/1808.04920 (2018).
25. Holt, M., Harder, R., Winarski, R. & Volker, R. Nanoscale hard D-ray microscopy methods for materials studies. *Annu. Rev. Mater. Sci.* **43**, 183–211 (2013).
26. Hruszkewycz, S. O. et al. High-resolution three-dimensional structural microscopy by single-angle Bragg ptychography. *Nat. Mater.* **16**, 244–251 (2017).
27. Pateras, A. et al. Mesoscopic elastic distortions in GaAs quantum dot heterostructures. *Nano. Lett.* **18**, 2780–2786 (2018).
28. Falk, A. L. et al. Polytype control of spin qubits in silicon carbide. *Nat. Commun.* **4**, 1819 (2013).
29. Falk, A. L. et al. Electrically and mechanically tunable electron spins in silicon carbide color centers. *Phys. Rev. Lett.* **112**, 187601 (2014).
30. Udvarhelyi, P., Shkolnikov, V. O., Gali, A., Burkard, G. & Pályi, A. Spin–strain interaction in nitrogen-vacancy centers in diamond. *Phys. Rev. B* **98**, 075201 (2018).
31. Toyli, D. M., Weis, C. D., Fuchs, G. D., Schenkel, T. & Awschalom, D. D. Chip-scale nanofabrication of single spins and spin arrays in diamond. *Nano. Lett.* **10**, 3168–3172 (2010).
32. Klimov, P. V., Falk, A. L., Buckley, B. B. & Awschalom, D. D. Electrically driven spin resonance in silicon carbide color centers. *Phys. Rev. Lett.* **112**, 087601 (2014).
33. Doherty, M. W. et al. Theory of the ground-state spin of the NV^- center in diamond. *Phys. Rev. B* **85**, 205203 (2012).
34. Klimov, P. V., Falk, A. L., Christle, D. J., Dobrovitski, V. V. & Awschalom, D. D. Quantum entanglement at ambient conditions in a macroscopic solid-state spin ensemble. *Sci. Adv.* **1**, 1501015 (2015).
35. Lee, K. W. et al. Strain coupling of a mechanical resonator to a single quantum emitter in diamond. *Phys. Rev. Appl.* **6**, 034005 (2016).
36. Chen, H. Y., MacQuarrie, E. R. & Fuchs, G. D. Orbital state manipulation of a diamond nitrogen-vacancy center using a mechanical resonator. *Phys. Rev. Lett.* **120**, 167401 (2018).
37. MacQuarrie, E. R., Otten, M., Gray, S. K. & Fuchs, G. D. Cooling a mechanical resonator with nitrogen-vacancy centers using a room temperature excited state spin–strain interaction. *Nat. Commun.* **8**, 14358 (2017).
38. Barson, M. S. J. et al. Nanomechanical sensing using spins in diamond. *Nano. Lett.* **17**, 1496–1503 (2017).
39. Awschalom, D. D., Hanson, R., Wrachtrup, J. & Zhou, B. B. Quantum technologies with optically interfaced solid-state spins. *Nat. Photon.* **12**, 516–527 (2018).
40. Udvarhelyi, P. & Gali, A. *Ab initio* spin–strain coupling parameters of divacancy qubits in silicon carbide. *Phys. Rev. Appl.* **10**, 05410 (2018).
41. Bennett, S. D. et al. Phonon-induced spin–spin interactions in diamond nanostructures: application to spin squeezing. *Phys. Rev. Lett.* **110**, 156402 (2013).
42. Kepesidis, K. V., Bennett, S. D., Portolan, S., Lukin, M. D. & Rabl, P. Phonon cooling and lasing with nitrogen-vacancy centers in diamond. *Phys. Rev. B* **88**, 064105 (2013).

Acknowledgements

The devices and experiments were supported by the Air Force Office of Scientific Research; material for this work was supported by the Department of Energy (DOE). SXDM measurements were performed at the Hard X-ray Nanprobe Beamline, operated by the Center for Nanoscale Materials at the Advanced Photon Source, Argonne National Laboratory (contract no. DE-AC02-06CH11357). S.J.W. and K.J.S. were supported by the NSF GRFP, C.P.A. was supported by the Department of Defense through the NDSEG Program, and M.V.H., F.J.H., A.N.C., G.G. and D.D.A. were supported by the DOE, Office of Basic Energy Sciences. This work made use of the UChicago MRSEC (NSF DMR-1420709) and Pritzker Nanofabrication Facility, which receives support from the SHyNE, a node of the NSF's National Nanotechnology Coordinated Infrastructure (NSF ECCS-1542205). The authors thank P. J. Duda, P. V. Klimov, P. L. Yu, S. A. Bhave, H. Seo and N. Schine for insightful discussions and B. B. Zhou, S. Bayliss and A. L. Yeats for careful reading of the manuscript.

Author contributions

S.J.W. fabricated devices. S.J.W. and G.W. performed the experiments and data analysis. C.P.A. and A.B. processed materials. H.M. and M.Y. performed DFT calculations. K.J.S. and G.K. helped with device characterization. M.V.H. executed X-ray imaging experiments. F.J.H., A.N.C., D.I.S., G.G. and D.D.A. advised on all efforts. All authors contributed to discussions and production of the manuscript.

Competing interests

The authors declare no competing interests.

Additional information

Supplementary information is available for this paper at https://doi.org/10.1038/s41567-019-0420-0.

Reprints and permissions information is available at www.nature.com/reprints.

Correspondence and requests for materials should be addressed to D.D.A.

Methods

Sample fabrication. The substrate was an on-axis, high-purity semi-insulating 4H-SiC commercial wafer (Cree Inc. serial no. W4TRF0R-0200). Defects were created in the 4H-SiC wafer by carbon-12 implantation with a dose of $10^{12}\,cm^{-2}$ at 170 keV and 7° tilt, which generated vacancies ~300 nm deep calculated using the Stopping and Range of Ions in Matter software; however, there was a high defect density in the SiC bulk from material growth. After annealing the wafer at 900 °C in N_2 for 2 h, the substrate was then cleaned sequentially with organic solvents, nanostrip and HF BOE before AlN was sputtered 500 nm thick on the wafer Si face by OEM Group Inc. The sputtered AlN layer had a film stress of −42 MPa and a rocking curve of 1.52° full-width at half-maximum on the AlN [0002] X-ray diffraction peak. The interdigitated transducer, consisting of 80 finger pairs with a window at the SAW focus spanning 3 wavelengths of missing fingers, was fabricated with 10 nm Ti and 150 nm Al. The Ti/Al and AlN device layers were each dry-etched by inductively coupled plasma (ICP) with 10 sccm Ar, 30 sccm Cl_2 and 30 sccm BCl_3, 400 W ICP power. AlN grooves (650 strips for each grating) in all SAW devices were etched nominally 180 nm deep.

The SAW resonator for spin transitions for Figs. 1, 3 and 4 was oriented longitudinally (SAW propagation direction) along $[\bar{1}\bar{1}20]$, and the resonator for Fig. 2 was oriented along $[1\bar{1}00]$. The x, y, z crystal directions are $[\bar{1}\bar{1}20]$, $[1\bar{1}00]$ and $[0001]$, respectively. Both devices had Gaussian geometry parameters $\lambda = 12\,\mu m$ and $w_0 = 2\lambda$, containing 80 electrode finger pairs and 650 grating strips. All interdigitated transducer electrodes and grating strips were overlapped $3\sigma = 3w/\sqrt{2}$ in the transverse direction, where w is the Gaussian spot size[43] along the axis of SAW propagation, while electrodes were apodized by only 2σ. Since the X-ray imaging experiments require specific frequencies for stroboscopic X-ray diffraction, the results in Fig. 1d,e used a similar transducer geometry and without AlN grooves for increased frequency bandwidth. This transducer was less impedance matched to 50 Ω compared to the Gaussian SAW resonators. Figure 1d,e used a Gaussian transducer with $\lambda = 19.03\,\mu m$, $w_0 = 1.25\lambda$ and 120 electrode finger pairs, yielding an interdigitated transducer centre frequency $f_0 \approx 352$ MHz with 1 MHz bandwidth. This was purposefully matched to an integer multiple of the Advanced Photon Source electron bunch frequency (~88 MHz) at Argonne National Laboratory.

Measurements. All divacancy spin manipulation experiments in this study were carried out in a closed-cycle cryostat from Montana Instruments Corp. operated with the sample temperature at 30 K. The sample is illuminated using 405 nm and 976 nm laser diodes, with the 405 nm acting as a charge-state reset[44] for neutral divacancies and 976 nm for exciting photoluminescence (>1,000 nm) and initializing the spin state. For pulsed laser experiments, the 976 nm laser is modulated using an acousto-optic modulator (<50 ns rise time), while the 405 nm laser diode is directly modulated by a current driver (250 kHz bandwidth). Emitted photoluminescence was separated by a dichroic and passed through a 1,000-nm long-pass filter, and then collected into a 62.5-μm-core optical fibre. Measurements were realized with an InGaAs photodiode at 1 kHz bandwidth, combined with a lock-in amplifier set at a reference frequency of ~400 Hz for all experiments.

Spin ensembles of divacancies near the Gaussian resonator's beam waist (defined by the acoustic focal spot w_0) are initialized and read out optically. To tune the ground-state spin sublevels, we use a combination of a permanent magnet and a wire loop on a printed circuit board to produce static magnetic fields (B_0) oriented along the 4H-SiC c axis. A coplanar waveguide behind the sample provides microwaves for in-plane magnetic spin control.

Data availability

All data are available upon request to the corresponding author.

References

43. Siegman, A. E. *Lasers* (University Science Books, Sausalito, 1986).
44. Wolfowicz, G. et al. Optical charge state control of spin defects in 4H-SiC. *Nat. Commun.* **8**, 1876 (2017).